Sensors and Materials, Vol. 29, No. 4 (2017) 397–404
MYU Tokyo

S & M 1332

Electrical Properties of Nanocrystalline Strontium Barium Niobate Thin Films Deposited at Room Temperature

Hsueh-Feng Hung, Cheng-Fu Yang,[1] and Chia-Ching Wu[2*]

Department of Beauty Science, Meiho University, Taiwan, R.O.C.
[1]Department of Chemical and Materials Engineering, National University of Kaohsiung, Kaohsiung, Taiwan, R.O.C.
[2]Department of Electronic Engineering, Kao Yuan University, Kaohsiung, Taiwan, R.O.C.

(Received August 30, 2016; accepted January 6, 2017)

Keywords: strontium barium niobate, nanometer grain size, ferroelectric properties, thin film

Strontium barium niobate ($Sr_{0.3}Ba_{0.7}Nb_2O_6$, SBN) thin films of good quality were deposited on silicon substrates by radio frequency magnetron sputtering at room temperature and under different deposition pressures. The surface morphology and thicknesses of the SBN thin films were characterized by field emission scanning electron microscopy, and it was found that the thickness increased as the deposition pressure increased. The nanocrystalline structure of the SBN thin films was observed for 10 and 30 mTorr deposition pressures. Ferroelectric properties were determined by measuring leakage current density, capacitance, and polarization. For the SBN thin film deposited at 30 mTorr, the remnant polarization, saturation polarization, and coercive field values were 20.67 μC/cm^2, 12.23 μC/cm^2, and 1.73 MV/cm, respectively.

1. Introduction

Ferroelectric materials are an important class of materials whose main characteristic is the presence of a spontaneous polarization that can be changed with an external electric field.[1] Ferroelectric materials with switching behavior of polarization have attracted much attention for their use in novel electronic devices, such as nonvolatile high-density memory applications. For example, the electrical switching of ferroelectric materials between two stably polarized states gives rise to the binary codes for nonvolatile ferroelectric random access memories (FeRAMs).[2] It has been experimentally found that FeRAMs are extremely durable, meaning that their polarization state can be changed as many as 10^{14} times without fatigue.[3] Ferroelectrics include titanates, zirconates, and niobates, and they can be classified on the basis of their structural type.

In February 2003, the European Union adopted the Restriction of Hazardous Substances (RoHS) directive, limiting the use of certain hazardous substances in electrical and electronic equipment. Thus, developing environmentally friendly, lead-free-based ceramics to replace Pb-based ceramics has become one of the main goals in current research. $Sr_xBa_{1-x}Nb_2O_6$ is an attractive ferroelectric material, widely considered very useful in diverse device applications, including memory devices, waveguide devices, and others.[4,5] Sixty years ago, Magneli deduced the tungsten bronze composite structure. The tungsten bronze composite family is one of several ferroelectric materials to include niobates such as $Sr_xBa_{1-x}Nb_2O_6$.[6] However, so far, only a few studies have

*Corresponding author: e-mail: 9113718@gmail.com
http://dx.doi.org/10.18494/SAM.2017.1521

ISSN 0914-4935

focused on $Sr_xBa_{1-x}Nb_2O_6$-based thin films that have different compositions, with a view to further possible applications. $Sr_xBa_{1-x}Nb_2O_6$ presents a tetragonal or orthorhombic phase, depending on its composition and temperature. Investigation of $Sr_xBa_{1-x}Nb_2O_6$ ceramics using X-ray diffraction suggests that a morphotropic phase boundary (MPB) exists around the composites of $Sr_{0.25}Ba_{0.75}Nb_2O_6$, which is characterized by the coexistence of tetragonal and orthorhombic phases.[7] The $Sr_{0.2}Ba_{0.8}Nb_2O_6$ ceramic presents a tetragonal ferroelectric phase between 120 and 293 °C, an orthorhombic phase below 120 °C, and a tetragonal paraelectric phase above 293 °C.

In the past, $Sr_xBa_{1-x}Nb_2O_6$ thin films were prepared by several techniques, including sol-gel processing,[8,9] pulsed laser deposition (PLD),[10,11] and metalorganic chemical vapor deposition (MOCVD).[12,13] Recently, the preparation of SBN thin films by a chemical method based on a polymeric resin containing metallic ions has been proposed.[14] However, radio frequency (RF) magnetron sputtering is a simple method of depositing thin films.[15] In this work, $Sr_{0.7}Ba_{0.3}Nb_2O_6$ (SBN) thin films were obtained by an RF magnetron sputtering method at room temperature. The effect of deposition pressure on the crystallinity and ferroelectricity of SBN thin films was studied by scanning electron microscopy and X-ray diffraction (XRD), and by the analyses of leakage current, capacitance, and polarization.

2. Experimental Procedure

$SrCO_3$, $BaCO_3$, and Nb_2O_5 were mixed to form the SBN ceramic, which was then ball-milled with deionized water for 1 h. After drying and grinding, the powder was calcined at 1100 °C for 2 h, and formation of the tungsten bronze structure was confirmed from the XRD pattern. After grinding again, the calcined powder was uniaxially pressed in a steel die into a 2-inch disk, and the ceramic was sintered at 1350 °C in air for 2 h. The SBN thin films were deposited under various deposition pressures on a polished Si wafer of nominal resistivity (~1.0 Ω cm) by an RF sputtering. The deposition power was 100 W, and pure argon (Ar) was used as the reaction gas. The working distance between the substrate and the target was fixed at 10 cm. The structure of the SBN thin films at different deposition pressures was analyzed by XRD using CuKα radiation from a Rigaku rotating anode with an incident angle of 2°. Field emission scanning electron microscopy (FE-SEM) was used to study the surface morphologies of the deposited SBN thin films. The electrical properties of the SBN thin films were measured using metal-ferroelectric-metal (MFM) and metal-ferroelectric-insulation-semiconductor (MFIS) structures, as shown in Fig. 1. The aluminum (Al) top electrodes were deposited by electron beam evaporation on the SBN thin films, with a 1-mm-

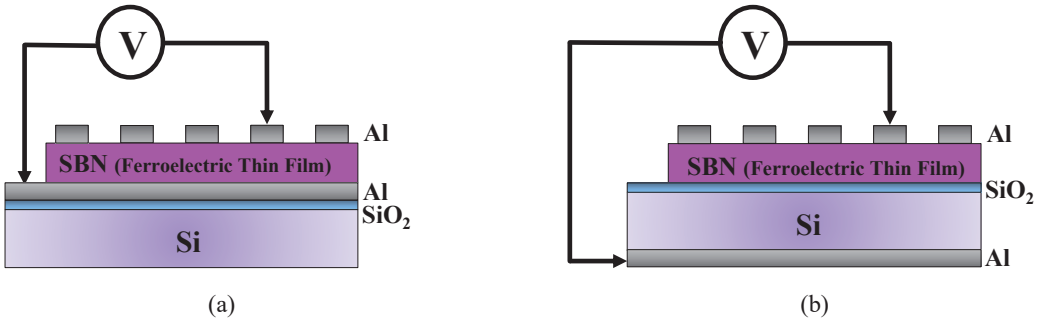

(a) (b)

Fig. 1. (Color online) Diagrams of (a) MFM and (b) MFIS structures.

diameter shadow mask, to form the MFM and MFIS structures. The leakage current density versus applied electric field (*J–E*) was measured for the MFIS structure using an HP 4156 semiconductor parameter analyzer. The MFIS structure was also used to measure capacitance versus voltage (*C–V*) using an HP 4294A precision impedance analyzer. All measurements were conducted at room temperature. The saturation polarization, remanent polarization, and coercive field properties of the MFM structure were measured using ferroelectric material test instruments.

3. Results and Discussion

Figure 2 shows surface FE-SEM images of the SBN thin films. It is evident that the SBN surface morphology varies markedly with the different sputtering pressures, as the results in Figs. 2(a) to 2(d) show. In the case of the SBN thin film deposited at 5 mTorr [Fig. 2(a)], the surface is smooth and no grain growth is observable. This is because at this low pressure, the mean free path between the substrate and target is longer and the kinetic energy of the sputtered particles arriving at the substrate surface is enhanced. The higher the kinetic energy, the more sputtered atoms with high surface mobility reach the substrate surface, creating a smoother SBN thin film.[16] As Fig. 2(b) shows, grain growth in the SBN thin films was improved at a deposition pressure of 8 mTorr. Figures 2(c) and 2(d) show the results for deposition pressures of 10 and 30 mTorr. As the SEM image shows, the SBN thin films have grain sizes of 3–10 nm and 7–16 nm, respectively. At higher deposition pressures, because of the shorter collisional mean free path of the particles, the sputtered atoms suffer multiple collisions before reaching the substrate; they cannot make proper arrangements on reaching the substrate owing to their reduced kinetic energies; hence, they form large grains during deposition.[17] Thus, the grain growth of the SBN thin films increases as the

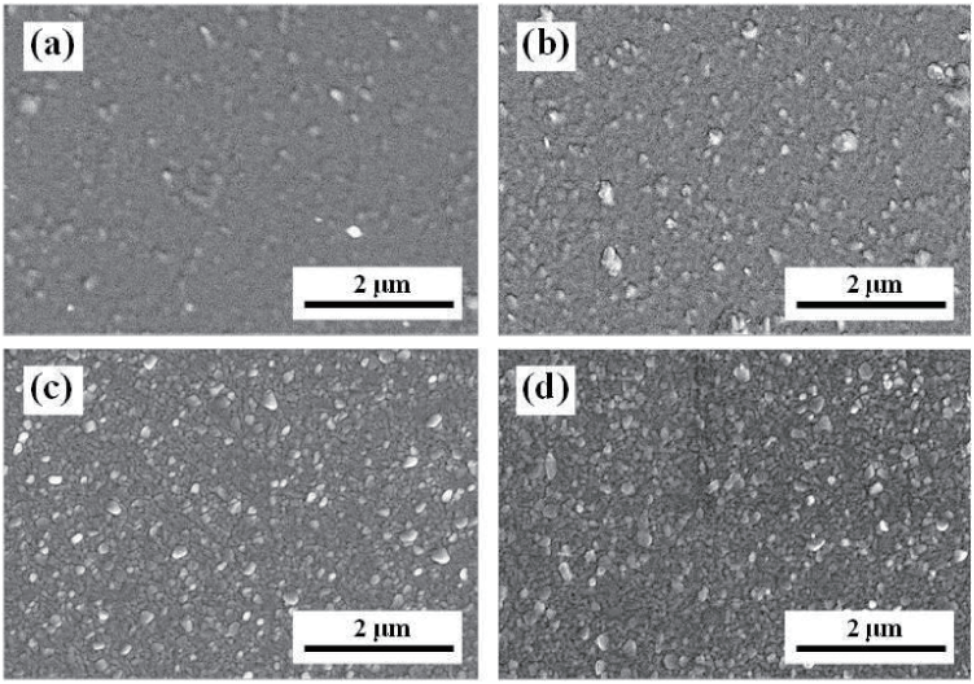

Fig. 2. Surface FE-SEM images of the SBN thin films deposited at different pressures: (a) 5, (b) 8, (c) 10, and (d) 30 mTorr.

deposition pressure increases from 5 to 30 mTorr. From these results, the deposition pressure at which the sputtering takes place has an important impact on the growth process of thin films.

The thickness of the SBN thin films also increases as the deposition pressure increases from 5 to 10 mTorr, as shown in Fig. 3. It is theorized that Ar ions remove SBN molecules from the surface of the SBN ceramic target. When the deposition pressure is lower (5 mTorr), there are fewer Ar ions to remove SBN molecules, leading to a lower deposition ratio for the SBN thin film. As the deposition pressure is increased from 5 to 10 mTorr, more Ar ions bomb the surface of the SBN ceramic target. Because of that, more SBN particles deposit on the substrate and the thickness of the SBN thin films increases. As the sputtering pressure is increased to 30 mTorr, the mean free path of the sputtered particles becomes shorter and the energy of the sputtered particles arriving at the substrate surface falls due to collisions with Ar ions. Less energy is left for substrate surface diffusion, so the sputtered particles have less surface mobility. The thickness of the SBN thin films therefore decreased to 181.3 nm as the deposition pressure increased from 10 to 30 mTorr.

Figure 4 shows the effect of deposition pressure on the thickness and grain sizes of the SBN thin films. At deposition pressures of 5, 8, 10, and 30 mTorr, the thicknesses of the SBN thin films were 127.02, 236.43, 450.53, and 181.27 nm, respectively. The grain sizes of the SBN thin films were 6.9, 14.8, 20.8, and 60.1 nm, respectively. Results from XRD analysis of the SBN thin films deposited at different pressures are shown in Fig. 5. All SBN thin films showed an amorphous structure because they were deposited at room temperature. Crystalline peaks at 38.5 and 44.7° were observed in the Al electrode, and the diffraction peaks' intensities decreased as the deposition pressure increased from 5 to 10 mTorr. This result confirms that the thickness of the SBN thin films increases as the deposition pressure increases from 5 to 10 mTorr (as shown in Figs. 3 and 4).

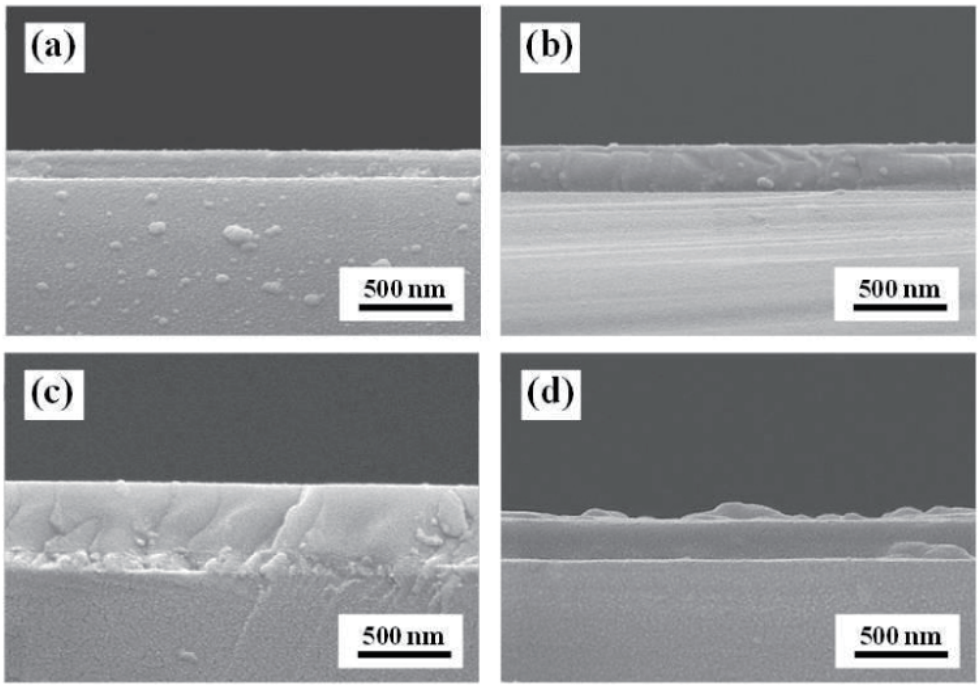

Fig. 3. Cross-sectional FE-SEM images of the SBN thin films deposited at different pressures: (a) 5, (b) 8, (c) 10, and (d) 30 mTorr.

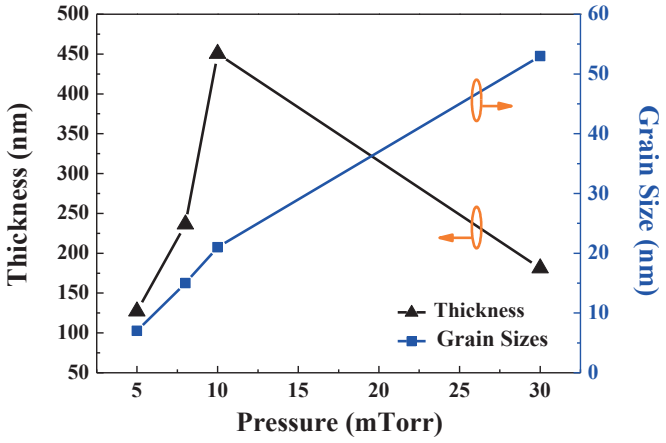

Fig. 4. (Color online) Thickness and grain size of the SBN thin films deposited at different pressures.

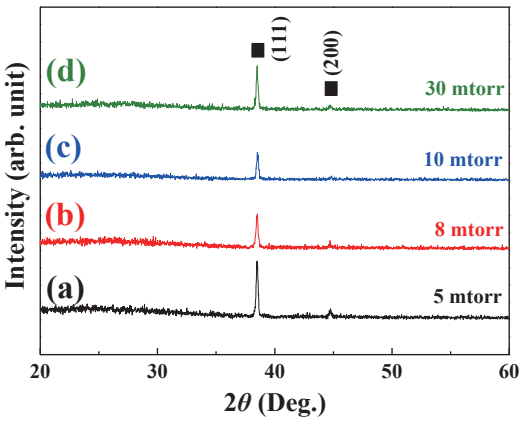

Fig. 5. (Color online) XRD analysis of the SBN thin films deposited at different pressures: (a) 5, (b) 8, (c) 10, and (d) 30 mTorr. (The ■ symbol indicates the Al phase.)

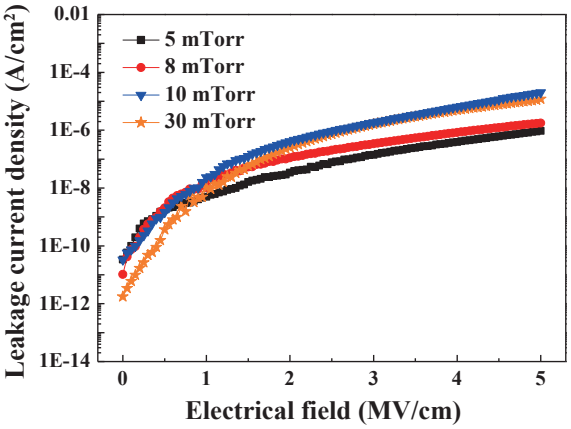

Fig. 6. (Color online) *J–E* curves of the SBN thin films deposited at different pressures.

Figure 6 shows the *J–E* curves of the SBN thin films with the MFM structure as a function of deposition pressure. The leakage current density of the SBN thin films increased slightly as the deposition pressure increased from 5 to 10 mTorr. There are many factors that affect the leakage current densiny, including the thickness of and defects in the deposited SBN thin films. This is due to the Ar atmosphere, which means that more oxygen vacancies and defects exist in the SBN thin film at higher deposition pressures. To explain these results and explore the effects of oxygen vacancy and defects on SBN thin films, the leakage current density versus electrical field curves were fitted to Schottky emission or Poole-Frenkel mechanism models to characterize the improvement in the leakage current of the SBN thin films.[18,19] When the deposition pressure was 30 mTorr, the leakage current density was slightly lower than that at 10 mTorr. When the deposition pressure was 5 to 30 mTorr, the leakage current density first increased with the increase in applied electrical field, then became saturated at 2.03×10^{-9}, 3.05×10^{-9}, 7.78×10^{-9}, and 3.96×10^{-9} A/cm^2 as the electrical field increased from 0 to 0.5, 0.56, 0.7, and 0.68 MV/cm, respectively.

The *C–V* curves of the SBN thin films were measured with an HP 4294 impedance analyzer for the MFIS structure; the results are shown in Fig. 7. The applied voltages were first changed from −20 to 20 V and then returned to −20 V. The capacitance of the SBN thin films increased from 33 to 34 pF, from 52 to 55 pF, from 88 to 95 pF, and from 63 to 89 pF at deposition pressures of 5, 8, 10 and 30 mTorr, respectively. The increase in the capacitance of the SBN thin films is considerable because the grain size and crystalline orientation increase, causing an increase in polarization. The memory windows of the SBN thin films were not observable at a deposition pressure of 5 mTorr. As the pressure increased from 8 to 10 to 30 mTorr, the memory windows of the SBN thin films were 6.2, 5.1, and 9.7 V, respectively. The memory window is defined as the flat-band voltage shift in the aligned directions of the *C–V* curves.[20] We compared the relationships between the memory windows and the leakage current densities of the SBN thin films shown in Figs. 6 and 7. For the SBN thin films deposited at 10 mTorr, as we know, for the ferroelectric thin films, the larger leakage current density causes less charge to be residual in the ferroelectric layer and then leads to a smaller memory window. In addition, when the negative voltage is biased on the ferroelectric thin film, holes accumulate at the SiO_2–Si interface. If there are defects and holes tunnel into the SiO_2-Si interface and through the SiO_2 layer, this causes the *C–V* curve to change from clockwise to counterclockwise, decreasing the memory window.[21]

Figure 8 shows the polarization versus applied electrical field (*P–E*) curves of the SBN thin films with the MFM structure. The development of hysteresis loops in the SBN thin films confirms the ferroelectric nature. The hysteresis loops were not found in the SBN thin films deposited at 5 and 8 mTorr. The SBN thin films deposited at 10 mTorr had the maximum remnant polarization (*Pr*), saturation polarization (*Ps*), and minimum coercive field (*Ec*) of 2.68 μC/cm², 8.71 μC/cm², and 0.57 MV/cm, respectively. The *Pr*, *Ps*, and *Ec* values of the 30-mTorr-deposited SBN thin films were 20.67 μC/cm², 12.23 μC/cm² and 1.73 MV/cm, respectively. The *Pr*, *Ps*, and *Ec* values of the SBN thin film deposited at 30 mTorr and room temperature were larger than those in other reports.[22–24] These results suggest that we have improved the remnant polarization of the SBN thin films with a deposition pressures of 30 mTorr.

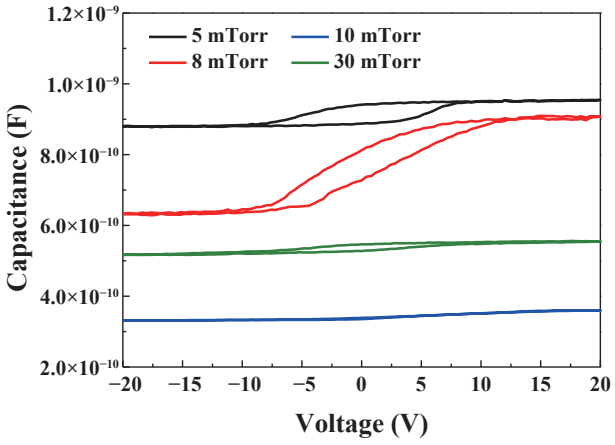

Fig. 7. (Color online) *C–V* curves of the SBN thin films at different deposition pressures.

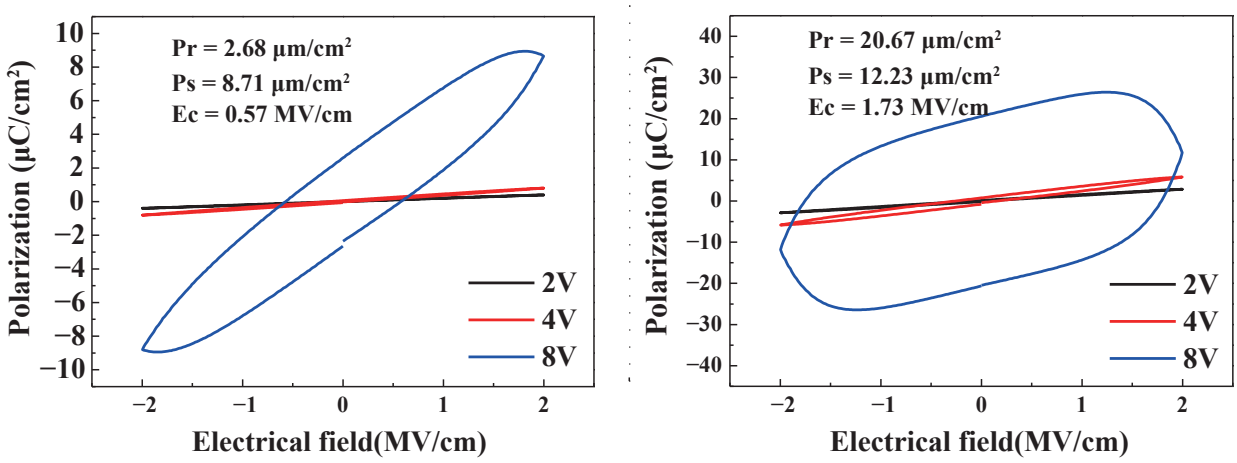

(a) (b)

Fig. 8. (Color online) *P–E* curves of the SBN thin films with different deposition pressures under different applied voltages: (a) 10 and (b) 30 mTorr.

4. Conclusions

In this study, we employed RF sputtering to deposit SBN thin films. When 10 and 30 mTorr were used as the deposition pressures, the grain size distributions of the SBN thin films were 3–10 and 6–15 nm, respectively. As the deposition pressure was increased from 8 to 30 mTorr, the memory windows of the SBN thin films were 6.2, 5.1, and 9.7 V, respectively. For the SBN thin film deposited at 10 mTorr, a smaller memory window was obtained because larger leakage current density led to less residual charge in the ferroelectric layer. In addition, defects occurred, and holes tunneled through the SiO_2–Si interface into the SiO_2 layer, causing the memory window of the SBN thin films to decrease. The *Pr*, *Ps*, and *Ec* values of the SBN thin film deposited at 30 mTorr were larger than in other reports. In the future, the SBN thin films will play an important role in applications for nonvolatile memory devices.

Acknowledgements

The authors acknowledge the financial support of the Ministry of Science and Technology, R.O.C. with contract Nos. MOST 104-2221-E-390-013-MY2, MOST 105-2221-E-244-014, and MOST 105-2221-E-244-013.

References

1 J. Valasek: Phys. Rev. **17** (1921) 475.
2 S. Das and J. Appenzeller: Nano Lett. **11** (2011) 4003.
3 R. Moazzami: Semicond. Sci. Techniol. **10** (1995) 375.
4 S. B. Xiong, Z. M. Ye, X. Y. Chen, X. L. Guo, S. N. Zhu, Z. G. Liu, C. Y. Lin, and Y. S. Jin: Appl. Phys. A **67** (1998) 313.
5 Y. H. Xu, C. J. Chen, R. Xu, and J. D. Mackenzie: Phys. Rev. B **44** (1991) 35.
6 A. Magneli: Arkiv för Kemi **1** (1949) 213.

7 S. Nishiwaki, J. Takahashi, K. Kodaira, and M. Kishi: Jpn. J. Appl. Phys. **35** (1996) 5137.
8 S. B. Majumder, P. S. Dobal, S. Bhaskar, and R. S. Katiyar: Ferroelectrics **241** (2000) 287.
9 S. Hirano, T. Yogo, K. Kikuta, and K. Ogiso: J. Amer. Ceram. Soc. **75** (1992) 1697.
10 S. S. Thöny, K. E.Youden, J. S. Harris Jr., and L. Hesselink: Appl. Phys. Lett. **65** (1994) 2018.
11 X. L. Guo, Z. G. Liu, X. Y. Chen, S. N. Zhu, S. B. Xiong W. S. Hu, and C. Y. Lin: J. Phys. D **29** (1996) 1632.
12 M. Lee and R. S. Feigelson: J. Cryst. Growth **180** (1997) 220.
13 M. J. Nystrom, B. W. Wessels, W. P. Lin, G. K. Wong, D. A. Neumayer, and T. J. Marks: Appl. Phys. Lett. **66** (1995) 1726.
14 R. G. Mendes, E. B. Araújo, H. Klein, and J. A. Eiras: J. Mater. Sci. Lett. **18** (1999) 1941.
15 F. H. Wanga, C. F. Yang, and M. C. Liu: J. Sci. Innovation **6** (2016) 7.
16 W. Maass, B. Ocker, J. Langer, and Y. Hua: Proc. Int. Conf. Memory Technology and Design **123** (2005).
17 H. Toku, R. S. Pessoa, H. S. Maciel, M. Massi, and U. A. Mengui: Brazilian J. Phys. **40** (2010) 340.
18 Y. K. Wang, T. Y. Tseng, and L. Pang: Appl. Phys. Lett. **80** (2002) 3790.
19 R. Balachandran, B. H. Ong, H. Y. Wong, K. B. Tan, and M. Muhamad Rasat: Int. J. Electrochem. Sci. **7** (2012) 11895.
20 H. T. Lue, C. J. Wu, and T. Y. Tseng: IEEE Trans. Electro. Devices **49** (2002) 1790.
21 H. Sugiyama, T. Nakaiso, Y. Adachi, M. Noda, and M. Okuyama: J. Appl. Phys. **39** (2000) 2131.
22 K. Lee, B. R. Rhee, and C. Lee: J. Korean Phys. Soc. **38** (2001) 723.
23 I. S. Kim, Y. M. Kim, I. H. Choi, S. I. Kim, Y. H. Kim, D. C. Yoo, J. Y. Lee, and C. S. Son: J. Korean Phys. Soc. **45** (2004) 1275.
24 J. Zhaoa, Y. Lib, X. Liua, H. Zhanga, and B. Wang: Mater. Lett. **58** (2004) 1456.